A Method for Computing the Partial Derivatives of Experimental Data

Y. Leong Yeow, Jordan Isac, and Fathullah A. Khalid
Dept. of Chemical and Biomolecular Engineering, The University of Melbourne, Parkville, VIC 3010, Australia

Yee-Kwong Leong
Dept. of Mechanical Engineering, University of Western Australia, Crawley, WA 6009, Australia

A. S. Lubansky
Dept. of Engineering Science, University of Oxford, Oxford OX1 3PJ, U.K.

DOI 10.1002/aic.12236
Published online April 5, 2010 in Wiley Online Library (wileyonlinelibrary.com).

This article describes a procedure for obtaining the partial derivatives of experimental data that depend on two independent variables. The starting equation is an ill-posed integral equation of the first kind. Tikhonov regularization is used to keep noise amplification under control. Implementation of the computation steps is described and the performance of the procedure is demonstrated by four practical examples. © 2010 American Institute of Chemical Engineers *AIChE J,* 56: 3212–3224, 2010
Keywords: partial derivative, integral equation, inverse problem, Tikhonov regularization, data interpolation

Introduction

Scientific and engineering investigations often require the evaluation of the derivatives of experimental data. Computing derivatives by any of the commonly adopted techniques, such as finite difference approximation or analytical differentiation of globally or locally fitted functions, is unlikely to lead to reliable results. This is because differentiation is an inherently ill-posed inverse problem. The unavoidable noise in the data will be amplified during the computation of the derivatives.[1] Tikhonov regularization is a specialized technique for handling ill-posed inverse problems. Lubansky et al.[2] applied this technique to evaluate the ordinary derivatives of experimental data that depend on a single independent variable. The built-in regularization parameter in Tikhonov regularization is able to keep noise amplification under control. This technique also has the advantage that it does not require the functional relationship between the dependent and independent variables to be known or specified.

Correspondence concerning this article should be addressed to Y. L. Yeow at yly@unimelb.edu.au.

The present article describes a procedure for obtaining the partial derivatives of experimental data when the dependent variable is a function of two independent ones. Examples of such data include variation of the volume percent of an agglomerating suspension with floc size and time, the dependence of specific volume of a binary solution on composition and temperature, the change in the pressure of a fluid with density and temperature. The procedure to be developed also relies on Tikhonov regularization to keep noise amplification under control but starts from a governing equation that is entirely different from that used by Lubansky et al. It also involves significantly different computation steps which are considerably more complicated.

For the purpose of describing the development of the new procedure, the two independent variables will be denoted generally by x and y and the dependent variable by z, i.e., $z = f(x, y)$. Apart from the general requirement that $f(x, y)$ be a well-behaved function that can be differentiated as many times as required this new procedure again does not require its functional form to be known or specified.

The input to the procedure is a set of experimental data in the general form $\{[x_1^M, y_1^M, z_1^M]^T, [x_2^M, y_2^M, z_2^M]^T, \ldots [x_i^M, y_i^M, z_i^M]^T, \ldots [x_{N_D}^M, y_{N_D}^M, z_{N_D}^M]^T\}$. The superscript M is used here to

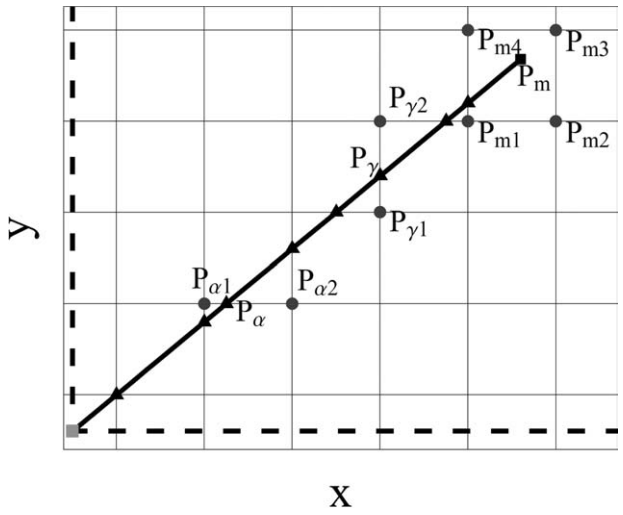

Figure 1. Representation of the derivatives at the intersection points (▲) of the integration path (—) with gridlines and at the measurement point (■) by that at the nearest grid points (●).

The integration path connects the reference point (■) at the lower left corner, on the boundary (— — —), of the measurement rectangle to the measurement point. Pα, Pγ, and Pm are represented by the linear interpolation of (Pα1 and Pα2), (Pγ1 and Pγ2), and (Pm1, Pm2, Pm3, and Pm4), respectively.

distinguish experimentally determined quantities from their computed counterparts, which will carry a superscript C. N_D is the number of points in the data set. These data points are arranged in ascending order of the independent variables (x, y). It is assumed that all the measurement points fall within the rectangle, the measurement rectangle, with (x_{ref}, y_{ref}) as its lower left corner and the last measurement point $(x_{N_D} y_{N_D})$ as its upper right corner. The coordinates (x_{ref}, y_{ref}) of the lower left corner, referred to as the reference point, is given by (Min$[x_i]$, Min$[y_i]$), $i = 1$ to N_D. See Figure 1. In most cases (x_{ref}, y_{ref}) is also the first data point (x_1, y_1) of the data set. In all the subsequent computation, the experimental data will be normalized using the following scaling factors $(x_{N_D} - x_{ref})$, $(y_{N_D} - y_{ref})$ and (Max$[z_i]$ − Min$[z_i]$), $i = 1$ to N_D in the x-, y-, and z-direction, respectively.

The introduction of a second independent variable brings with it a number of complications. The most obvious one is that there are now two first partial derivatives, $(\partial z/\partial x)_y$ and $(\partial z/\partial y)_x$, to be evaluated instead of just a single ordinary derivative dz/dx. This not only increases the computing load significantly but also the mathematical complexity of the problem compared to that for ordinary derivative. In the subsequent paragraphs, the two partial derivatives will be denoted by $p(x, y) \equiv (\partial z/\partial x)_y$ and $q(x, y) \equiv (\partial z/\partial y)_x$ The subscript showing which independent variable is being held fixed will be suppressed when that does not lead to confusion.

As general functions $p(x, y)$ and $q(x, y)$ are independent of one another. However, the mixed second derivatives of a well-behaved $f(x, y)$ satisfy the relationship $\partial((\partial z/\partial x)_y/\partial y)_x = \partial((\partial z/\partial y)_x/\partial x)_y$.[3] This gives rise to an equation relating $p(x, y)$ and $q(x, y)$ that has no counterpart when evaluating ordinary derivatives

$$(\partial p/\partial y)_x = \partial((\partial z/\partial x)_y/\partial y)_x = \partial((\partial z/\partial y)_x/\partial x)_y = (\partial q/\partial x)_y. \quad (1)$$

This condition has to be met even in practical situations where the physical interest is only in the first derivatives $p(x, y)$ and $q(x, y)$ and represents an added complication in the partial derivative problem.

In typical a experiment measurements may not be carried out at regularly spaced out independent variables (x, y) and consequently the measurement points (x_i, y_i), $i = 1$ to N_D can be irregularly distributed within the measurement rectangle. This adds to the complication in the representation of the data points and of the partial derivatives $p(x, y)$ and $q(x, y)$ at these points within the two-dimensional discretized measurement rectangle with all the attendant added computing overhead.

The governing equation and its discretization together with the computation steps of the new procedure will be described in the next section. This is followed by a section in which a series of examples are introduced to demonstrate the new procedure in action. These examples, apart from their practical interest, have been selected so that the partial derivatives generated by Tikhonov regularization can be checked against results obtained independently by other methods.

Governing Equation, Discretization, and Implementation

The line integral equation

The value of the dependent variable z_i at a general measurement point (x_i, y_i) is related to the partial derivatives $p(x, y)$ and $q(x, y)$ along the linear path **l** joining the reference point (x_{ref}, y_{ref}) to the general point (x_i, y_i) by the line integral

$$z_i^C = \int_{(x_{ref}, y_{ref})}^{(x_i, y_i)} \nabla z(x', y').d\mathbf{l} + z_{ref}^C = \int_{(x_{ref}, y_{ref})}^{(x_i, y_i)} p(x', y')dx' + \int_{(x_{ref}, y_{ref})}^{(x_i, y_i)} q(x', y')\, dy' + z_{ref}^C \quad \text{for } i = 1, 2, \ldots N_D. \quad (2)$$

z_i^C is the computed equivalent of the measured quantity z_i^M and z_{ref}^C is the computed value of z at (x_{ref}, y_{ref}). (x', y') that appear within the integrals are dummy variables representing a general point on the linear path **l**. Equation 2 can be regarded as an integral equation of the first kind to be solved, together with Eq. 1, for the unknown functions $p(x, y)$ and $q(x, y)$ and the unknown constant z_{ref}^C so that the computed and measured variables are in agreement. This equation is very different from the governing equation, based on a two-term Taylor series with integral-form remainder term, used by Lubansky et al.[2] in the ordinary derivative problem.

Discretized equations

For the purpose of formulating the computation steps, it is convenient to put the experimental data in the form of a

known column vector: $\mathbf{z}^{\mathrm{M}} = [z_1^{\mathrm{M}}, z_2^{\mathrm{M}}, \ldots z_i^{\mathrm{M}}, \ldots z_{N_{\mathrm{D}}}^{\mathrm{M}}]^{\mathrm{T}}$ and a known matrix with two columns: $[\mathbf{x}^{\mathrm{M}}, \mathbf{y}^{\mathrm{M}}] = [(x_1^{\mathrm{M}}, y_1^{\mathrm{M}}), (x_2^{\mathrm{M}}, y_2^{\mathrm{M}}), (x_i^{\mathrm{M}}, y_i^{\mathrm{M}}), \ldots (x_{N_{\mathrm{D}}}^{\mathrm{M}}, y_{N_{\mathrm{D}}}^{\mathrm{M}})]^{\mathrm{T}}$. The dimensionless measurement rectangle is discretized into $N_T = N_K \times N_K$ two-dimensional uniformly spaced grid points. To ensure accurate representation of the measured data, N_T is usually set to be much larger than N_{D}. In all the examples below, $N_K = 41$ and $N_T = 41 \times 41 = 1681$. The uniform discretization grid spacing will be denoted by Δ and the coordinates of the dimensionless discretization grid points by column vectors $\mathbf{x}^{\mathrm{C}} = [x_1^{\mathrm{C}} = 0, x_2^{\mathrm{C}}, \ldots x_j^{\mathrm{C}}, \ldots x_{N_T}^{\mathrm{C}} = 1]^{\mathrm{T}}$, $\mathbf{y}^{\mathrm{C}} = [y_1^{\mathrm{C}} = 0, y_2^{\mathrm{C}}, \ldots y_j^{\mathrm{C}}, \ldots y_{N_T}^{\mathrm{C}} = 1]^{\mathrm{T}}$ to distinguish them from the measurement points $[\mathbf{x}^{\mathrm{M}}, \mathbf{y}^{\mathrm{M}}]$. In general, these two sets of coordinate points do not coincide.

The numerical value of the unknown derivatives $p(x, y)$ and $q(x, y)$ at each of the discretization grid points will be denoted by the unknown column vectors $\mathbf{p} = [p_1, p_2, \ldots p_j, \ldots p_{N_T}]^{\mathrm{T}}$ and $\mathbf{q} = [q_1, q_2, q_j, \ldots q_{N_T}]^{\mathrm{T}}$. In terms of these discretized variables, Eq. 2 takes the form

$$z_i^{\mathrm{C}} = \sum_{j=1}^{N_T} A_{ij} p_j + \sum_{j=1}^{N_T} B_{ij} q_j + z_{\mathrm{ref}}^{\mathrm{C}} \quad \text{for } i = 1, 2, \ldots N_{\mathrm{D}} \tag{3}$$

or in matrix notation

$$\mathbf{z}^{\mathrm{C}} = \mathbf{A}\mathbf{p} + \mathbf{B}\mathbf{q} + \mathbf{1} z_{\mathrm{ref}}^{\mathrm{C}} = [\,\mathbf{A} \quad \mathbf{B} \quad \mathbf{1}\,] \begin{bmatrix} \mathbf{p} \\ \mathbf{q} \\ z_{\mathrm{ref}}^{\mathrm{C}} \end{bmatrix} = \mathbf{C}\mathbf{P}. \tag{4}$$

From Eq. 3 it is clear that $\mathbf{A}$ and $\mathbf{B}$ are $N_{\mathrm{D}} \times N_T$ matrices of known numerical coefficients arising from the approximation of the integrals in Eq. 2 by the trapezoidal rule. To arrive at these coefficients, the derivatives $p(x', y')$ and $q(x', y')$ at any intersection point of the linear path $\mathbf{l}$ with the discretization gridlines are expressed, by linear interpolation, in terms of the elements of $\mathbf{p}$ and of $\mathbf{q}$ closest to that point. See Figure 1. For a typical measurement point $(x_i^{\mathrm{M}}, y_i^{\mathrm{M}})$ that does not coincide with a grid point its $p(x_i^{\mathrm{M}}, y_i^{\mathrm{M}})$ and $q(x_i^{\mathrm{M}}, y_i^{\mathrm{M}})$ are again given by a linear combination of the appropriate elements of the $\mathbf{p}$ and $\mathbf{q}$ column vectors. $\mathbf{1}$ in Eq. 4 is a column vector with N_{D} elements each equal to unity.

In the final form of Eq. 4, to simplify the computation steps, the unknown column vectors $\mathbf{p}$ and $\mathbf{q}$ and the unknown constant $z_{\mathrm{ref}}^{\mathrm{C}}$ are treated as a single column vector with $(2N_T + 1)$ unknown elements and denoted by $\mathbf{P} = [p_1, p_2, \ldots p_j, \ldots p_{N_T}, q_1, q_2, \ldots q_j, \ldots q_{N_T}, z_{\mathrm{ref}}^{\mathrm{C}}]^{\mathrm{T}}$. $\mathbf{C}$ is the $N_{\mathrm{D}} \times (2N_T + 1)$ matrix formed by the concatenation of the matrices $\mathbf{A}$ and $\mathbf{B}$ and $\mathbf{1}$ to reflect the introduction of the combined unknown column vector $\mathbf{P}$.

$\mathbf{A}$ and $\mathbf{B}$ and, hence, $\mathbf{C}$ are sparse matrices. For example, in the ith row of $\mathbf{A}$ and $\mathbf{B}$ only those elements associated with the p_j and q_j of those discretization points that lie immediately next to the integration path are non zero with all the other elements being identically zero. The numerical value of the non-zero elements are, as explained above, given by linear interpolation, i.e., inversely proportional to their distances from the intersection point. The locations of these non-zero elements in $\mathbf{C}$ depend on how the N_T gird points are ordered and numbered.

Discretization of Eq. 1 leads to a finite difference equation of the form

$$\frac{p_{j^+} - p_{j^-}}{2\Delta} - \frac{q_{j^+} - q_{j^-}}{2\Delta} = 0, \tag{5}$$

for each and every interior discretization point (x_j, y_j). There are thus $(N_K - 2) \times (N_K - 2)$ of Eq. 5 to be met. Simple central difference has been used to approximate the first partial derivatives $(\partial p/\partial y)_x$ and $(\partial q/\partial x)_y$. p_{j^+} and p_{j^-} in Eq. 5 represent, in shorthand notation, the x partial derivative $(\partial z/\partial x)_y$ at the two immediate neighboring points $(x_j, y_j + \Delta)$ and $(x_j, y_j - \Delta)$ of (x_j, y_j). Similarly, q_{j^+} and q_{j^-} denote the y partial derivative $(\partial z/\partial y)_z$ at the neighboring points $(x_j + \Delta, y_j)$ and $(x_j - \Delta, y_j)$. When assembled, the $(N_K - 2) \times (N_K - 2)$ of Eq. 5 take the following form:

$$\mathbf{D}\mathbf{P} = \mathbf{0}. \tag{6}$$

The number zeros in the null column vector $\mathbf{0}$ and the number of rows in $\mathbf{D}$ are both equal to $(N_K - 2) \times (N_K - 2)$ corresponding to the number of internal points in the measurement rectangle. The number of columns in $\mathbf{D}$ is $2N_T + 1$, i.e., the total number of unknowns in the column vector $\mathbf{P}$. In each row of $\mathbf{D}$, according to the coefficients of Eq. 5, there are only four non-zero elements of either 1 or -1 with all the remaining elements being identically zero. The locations of the non-zero elements in $\mathbf{D}$ again depend the way the N_T grid points are numbered.

The unknowns $P_1, P_2, P_3, \ldots P_{2N_T+1}$ are required to minimize the following sums of squares

(1) $S_1 = [\mathbf{z}^{\mathrm{C}} - \mathbf{z}^{\mathrm{M}}]^{\mathrm{T}}[\mathbf{z}^{\mathrm{C}} - \mathbf{z}^{\mathrm{M}}]$;
(2) $S_2 = [\mathbf{D}\mathbf{P}]^{\mathrm{T}}[\mathbf{D}\mathbf{P}]$;
(3) S_3 = Sum of squares of $\partial^2 p(x, y)/\partial x^2$, $\partial^2 q(x, y)/\partial x^2$, $\partial^2 p(x, y)/\partial y^2$, and $\partial^2 q(x, y)/\partial y^2$ at the $(N_K - 2) \times (N_K - 2)$ interior discretization points together with that of $\partial^2 p(x, y)/\partial y^2$ and $\partial^2 q(x, y)/\partial y^2$ at the $2(N_K - 2)$ interior points of the two x-constant boundaries and that of $\partial^2 p(x, y)/\partial x^2$ and $\partial^2 q(x, y)/\partial x^2$ at the $2(N_K - 2)$ interior points of the two y-constant boundaries.

Condition (1) ensures that the z^{C} at the measurement points $(\mathbf{x}^{\mathrm{M}}, \mathbf{y}^{\mathrm{M}})$ approximates $\mathbf{z}^{\mathrm{M}}$ closely at the measurement points. This is the same as that imposed by Lubansky et al. in their computation of ordinary derivatives. Condition (2) enforces the equality of the two mixed second derivatives of $z = f(x, y)$. This has no equivalent in the ordinary derivative problem. Condition (3), following the general practice in Tikhonov regularization, ensures that the computed $p(x, y)$ and $q(x, y)$ do not show spurious fluctuations. Condition (3) together with the assumed well-behaved nature of $f(x, y)$ ensures that the sum of squares of the mixed second derivatives of $p(x, y)$ and $q(x, y)$ are also minimized. The total number of second derivatives involved in Condition (3) is thus $4(N_K - 2) \times (N_K - 2) + 2[2 \times 2\,(N_K - 2)] = 4N_K\,(N_K - 2)$.

It is necessary to restrict Conditions (2) and (3) to the interior points so that all the second derivatives of $p(x, y)$ and $q(x, y)$ that appear in them can be approximated by the finite

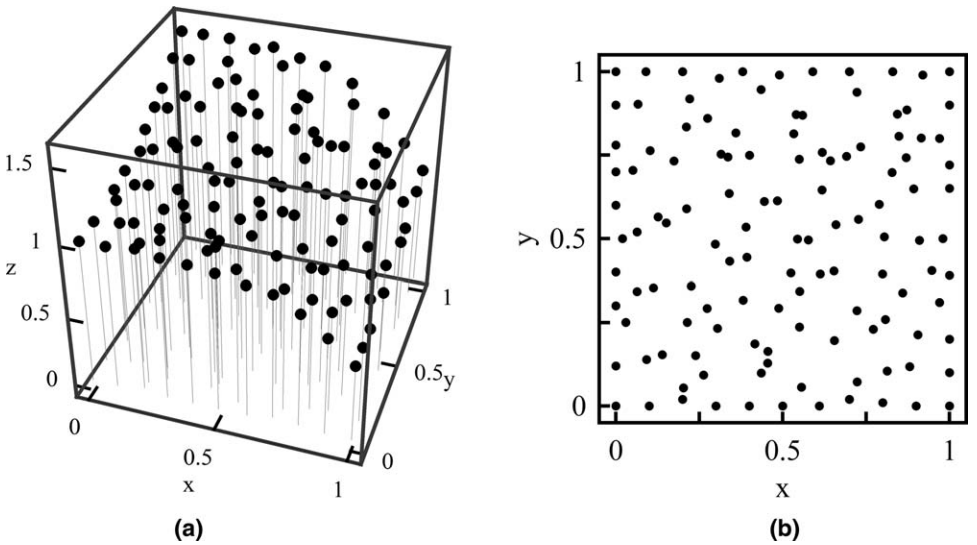

Figure 2. Synthetic data and measurement points.

(a) Exact data points based on $z = \cos(x^2)\cosh(y)$. (b) Irregularly distributed measurement points.

difference of the elements of the unknown column vector **P**. This avoids the necessity of including in **P** additional unknowns associated with grid points outside of the measurement rectangle.

Tikhonov regularization

In Tikhonov regularization, instead of minimizing (1), (2), and (3) separately, their linear combination $R = S_1 + S_2 + \lambda S_3$ is minimized.[1] λ is the regularization parameter that balances the two separate requirements. A large λ favors the smoothness condition while a small λ favors the accuracy condition and the equality of the mixed second derivatives of $f(x, y)$. The appropriate choice of λ depends on N_D and N_K and also on the noise level in the data and is not a physical property of the $f(x, y)$. It is, therefore, not useful, in fact may be confusing, to report the numerical value of λ used in the examples below. In this investigation, the choice of λ is guided by the simple and practical expectation that the average deviation of $\mathbf{z}^C$ from $\mathbf{z}^M(x, y)$ at the measurement points is of the same order of magnitude as the expected experimental error bar of $\mathbf{z}^M$. This is often referred to as the Morozov Principle[1] in mathematical texts.

For any λ, the unknowns $\mathbf{P} = [P_1, P_2, P_3, \ldots P_{2N_T+1}]$ that minimize R are given by[1]

$$\mathbf{P} = [\mathbf{E}^T\mathbf{E} + \lambda\boldsymbol{\beta}^T\boldsymbol{\beta}]^{-1}\mathbf{E}^T\mathbf{Z}^M_{ext}. \tag{7}$$

The composite matrix **E** and the extended column vector $\mathbf{Z}^M_{ext}$ are formed, respectively, by the joining of the matrices **C** and **D** in Eqs. 4 and 6 and of the known column vectors $\mathbf{z}^M$ and the null column vector **0** on the RHS of Eq. 6.

$$\mathbf{E} = \begin{pmatrix} \mathbf{C} \\ \mathbf{D} \end{pmatrix} \quad \text{and} \quad \mathbf{Z}^M_{ext} = \begin{pmatrix} \mathbf{z}^M \\ \mathbf{0} \end{pmatrix}. \tag{8}$$

The matrix $\boldsymbol{\beta}$ in Eq. 7 arises from the use of standard central finite difference to approximate the second derivatives $\partial^2 p/\partial x^2$, $\partial^2 p/\partial y^2$, $\partial^2 q/\partial x^2$, and $\partial^2 q/\partial y^2$ at each interior grid point of the measurement rectangle and selected members of these second derivatives at the interior points on the four boundaries. Each row of $\boldsymbol{\beta}$ has only three non-zero elements given by 1, -2, and 1 with all other elements being identically zero. As in the **C** and **D**, the locations of the non-zero elements depend on N_K and on the way the total set of N_T discretization points are numbered. Each row of $\boldsymbol{\beta}$ is terminated by an extra zero to allow for the incorporation of z^C_{ref} into **P**. This is because z^C_{ref} plays no role in the approximation of the second derivatives of $p(x, y)$ and $q(x, y)$. Thus, $\boldsymbol{\beta}$ has $4N_K \times (N_K - 2)$ rows and $(2N_T + 1)$ columns.

Equation 7 is the linear algebraic equation that converts the experimental data $\mathbf{z}^M$ into the partial derivatives $(\partial z/\partial x)_y$ and $(\partial z/\partial y)_x$ at a set of closely and regularly spaced discretization points. These partial derivatives allow the dependent variable at the measurement points $\mathbf{z}^C$ to be calculated with relative ease

$$\mathbf{z}^C = \mathbf{CP}. \tag{9}$$

Comparison of $\mathbf{z}^C$ with $\mathbf{z}^M$ provides an instant check on the partial derivatives. These partial derivatives can also be substituted into Eq. 2 and the two integrations performed numerically to back calculate the dependent variable z^C at any point of the measurement rectangle.

Applications and Results

Synthetic data

The discrete points in Figure 2a were generated by the well-behaved function $f(x, y) = \cos(x^2)\cosh(y)$ with the measurement points $[\mathbf{x}^M, \mathbf{y}^M]$ shown in Figure 2b. These measurement points, $N_D = 121$, are irregularly distributed within

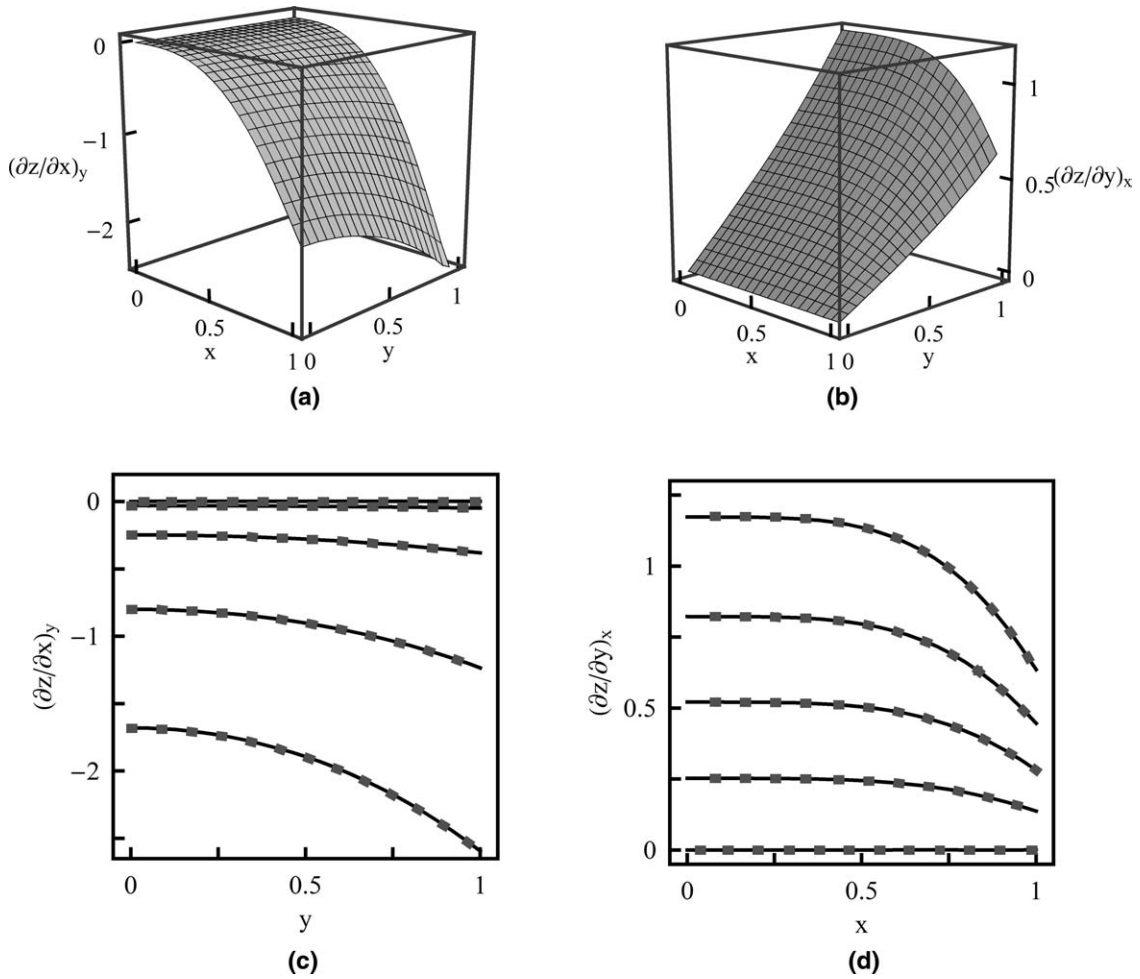

Figure 3. Computed and exact partial derivatives.

(a) Computed surface of $(\partial z/\partial x)_y$; (b) Computed surface of $(\partial z/\partial y)_x$; (c) Comparison of computed $(\partial z/\partial x)_y$ (——) against exact $(\partial z/\partial x)_y$ (···) at constant x. $x = 0$ (the top most curve), 0.25, 0.5, 0.75, and 1 (the lowest curve); (d) Comparison $(\partial z/\partial y)_x$ (——) with exact $(\partial z/\partial y)_x$ (···) at constant y. $y = 0$ (the lowest curve), 0.25, 0.5, 0.75, and 1 (the top most curve).

the square defined by (0, 0) and (1, 1). The generating function $f(x, y)$ allows the computed partial derivatives to be compared directly against their exact analytical counterparts.

The computed partial derivatives generated by Eq. 7 are shown as a continuous surface in Figures 3a, b. These surfaces are visually indistinguishable from the surfaces given by the exact partial derivatives (not shown). For a more quantitative comparison, the computed partial derivatives are shown as continuous curves in Figures 3c, d. x appears as a parameter in (c) and y as a parameter in (d). The large N_T allows the computed partial derivatives at the discretization points to be treated essentially as continuous curves. The corresponding curves based on the exact partial derivatives are shown as lighter broken curves on the same plot. The computed results agree with the exact partial derivatives to better than 0.01%. This is not very surprising as there is no error in the synthetic data and the function $z = f(x, y)$ used in this case is a relatively simple function with no local maxima or minima.

To test the performance of Eq. 7 in the presence of unavoidable measurement noise, $\pm 1\%$ random noise is now added to the data points in Figure 2a. The computed partial derivatives based on these "noisy" data are shown in Figures 4a, b as continuous curves. The broken curves are again the exact results. An immediate consequence of the added noise is that a much larger regularization parameter λ, compared to that in the earlier computation, is needed to suppress fluctuations in the partial derivatives. As expected, the deviation from the exact partial derivatives has increased. The average deviation of the two partial derivatives is significantly $>10\%$. This deviation becomes particularly large close to the boundaries of the measurement region. However, for many practical purposes, these computed results remain acceptable. It is interesting to note that the z^C (not shown) backed calculated from these partial derivatives is still in very good agreement with the exact function with an average deviation $<0.1\%$ indicating that the back-calculated z^C as a function of dependent variables x and y can be used to interpolate or to smooth the noisy data. The greatly amplified deviation observed in the computed partial derivatives is a manifestation of the ill-posed nature of the problem.

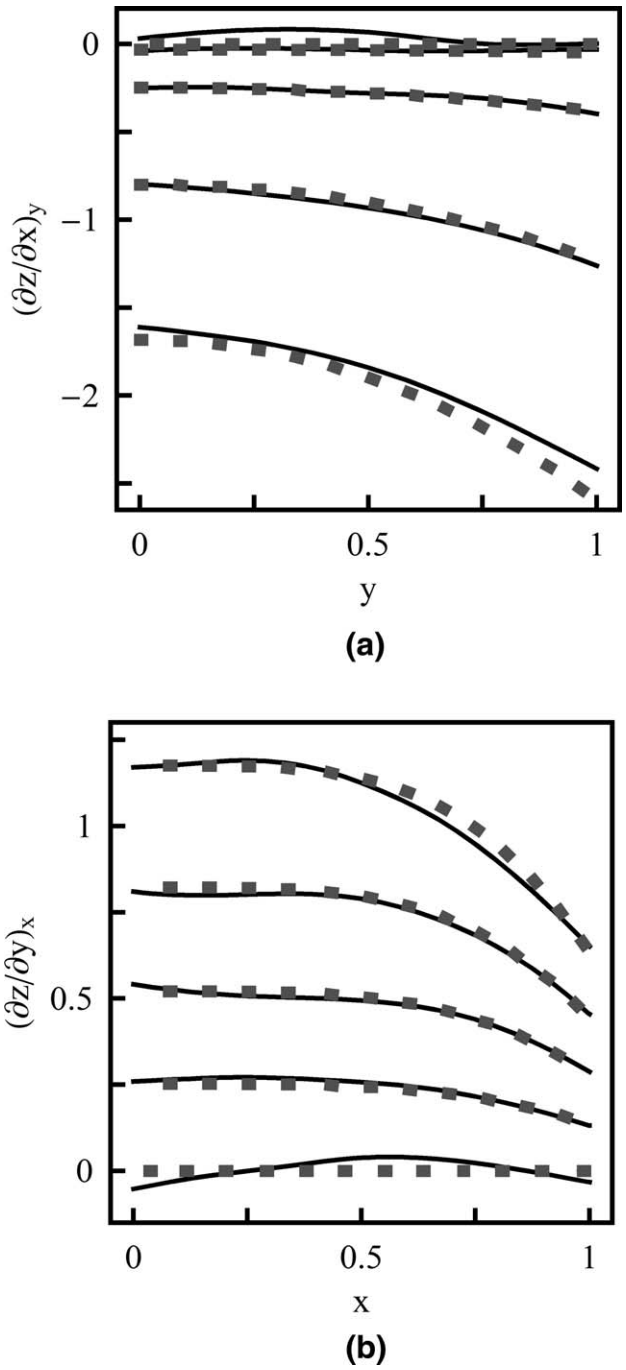

Figure 4. Computed derivatives based on noisy data and exact derivatives.

(a) Comparison of computed $(\partial z/\partial x)_y$ (——) with exact $(\partial z/\partial x)_y$ (- - -) at constant x. $x = 0$ (the top most curve), 0.25, 0.5, 0.75, and 1 (the lowest curve); (b) Comparison $(\partial z/\partial y)_x$ (——) with exact $(\partial z/\partial y)_x$ (- - -) at constant y. $y = 0$ (the lowest curve), 0.25, 0.5, 0.75, and 1 (the top most curve).

Particle size distribution in yeast cells agglomeration

Particle size distribution (PSD) is a key operation variable in particulate processes such as crystallization, suspension flocculation, and cell agglomeration. It shows the relationship between vol % and floc size L and how this changes with time t. Thus, a typical PSD takes the form of a function of two independent variables $\phi = f(t, L)$. For any t, $\delta\phi = f(t, L)\delta L$ gives the proportion of particles with size between $L - \delta L/2 < L < L + \delta L/2$. $f(t, L)$ is assumed to be a well-behaved function of t and L. $(\partial\phi/\partial t)_L$ gives the rate of growth of the proportion with size L while $(\partial\phi/\partial L)_t$ is a measure of its instantaneous variation with L. These partial derivatives are of practical interest and appear explicitly in the general population-balance equation used to describe particulate processes.[4] In this example, Eq. 7 will be used to obtain these partial derivatives based on a small set of experimental $\phi(t, L)$ data for cell agglomeration.

Han et al.[5] investigated the effects of different flocculants and their dosage on the agglomeration of yeast cells. Using a laser diffraction particle size analyzer, they monitored the vol % as a function of floc size, between 1 μm and 450 μm, of a yeast cell suspension during the agglomeration process. They recorded the PSD at regular intervals for an agglomeration time of over 10 min. A subset, 180 s $\leq t \leq$ 642 s and 28.25 μm $\leq L \leq$ 295.83 μm, of their large data collection will be used in this example. These are plotted, as discrete points, against floc size L, in Figure 5. There are 20 separate PSD data sets in these plots. The measurement time, fixed on a PSD, increases variously by 21 s to 42 s between sets. For each PSD, the particle size analyzer gives the vol % at the same 18 preselected floc sizes. $N_D = 360$ in this combined PSD data sets. For visual clarity, the PSD data points for consecutive measurement times are spread out on different plots.

The partial derivatives $(\partial\phi/\partial t)_L$ and $(\partial\phi/\partial L)_t$ given by Eq. 7 are shown in Figures 6a, b. λ has been adjusted to eliminate excessive fluctuations. These partial derivatives were substituted in Eq. 2 and the back-calculated $\phi^C(t, L)$ are shown as continuous curves in Figure 5. The curves are in reasonable agreement with the experimental data with an average deviation of around 8.2%. The deviation close to the boundaries of the measurement rectangle is again larger than that in the interior of the rectangle.

As a more direct check on the computed $(\partial\phi/\partial t)_L$ and $(\partial\phi/\partial L)_t$, the ϕ^M data points for a fixed t is treated as a function of L and that for a fixed L as a function of t. The Tikhonov regularization procedure of Lubansky et al. for data of a single dependent variable is now used to compute the ordinary derivatives $d\phi/dt$ and $d\phi/dL$. These ordinary derivatives are compared against the corresponding partial derivatives. Typical examples of such comparison are shown in Figures 6c, d. The partial derivatives and the corresponding ordinary derivatives are shown as continuous and lighter broken curves, respectively. Although the general trends of the partial and ordinary derivatives are in reasonable agreement, there are significant differences between them particularly near the boundaries of the measurement region. In view of the noise in the data, the differences in the two computation schemes and the large number of computing steps involved the observed level of agreement is considered as acceptable. Another possible contributory factor to the differences is the relatively small number of points, $N_D = 18$ in the constant t data and $N_D = 20$ in the constant L data, used in the computation of the ordinary derivatives compared to 360 used in the partial derivatives computation.

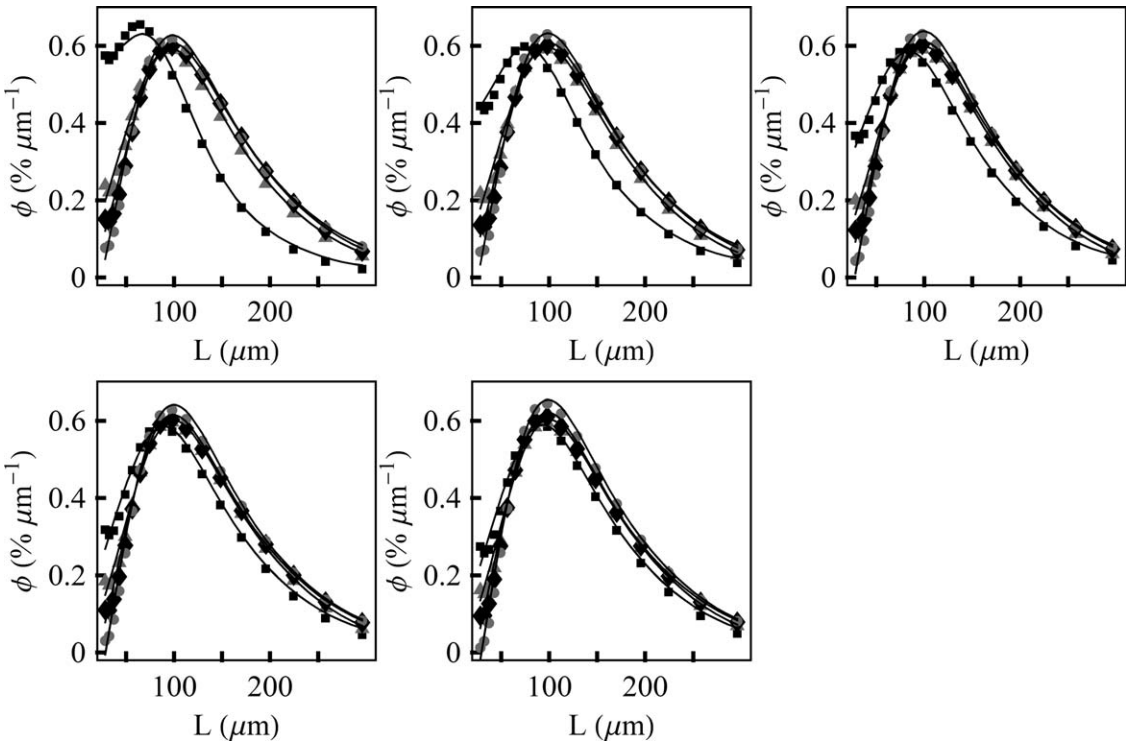

Figure 5. Experimental and computed PSD of yeast cells.

Discrete points are the experimental data of Han et al.[5] and continuous curves are back calculated from the partial derivatives given by Eq. 7. Upper row left to right: $t = 180$ (■), 284 (▲), 389 (◆), 494 (●) s; $t = 201$ (■), 305 (▲), 410 (◆), 515 (●) s; $t = 222$ (■), 326 (▲), 431 (◆), 557 (●) s. Lower row left and right: $t = 243$ (■), 347 (▲), 452 (◆), 600 (●) s; $t = 263$ (■), 368 (▲), 473 (◆), 642 (●) s.

Partial molar volume of MIPA

Mokraoui et al.[6] measured the density of aqueous monoisopropanolamine (MIPA) solutions with different mole fraction x_W of water. They reported the density data for a series of constant temperature T between 273.15 K and 353.15 K. Their raw data have been converted into specific volume v and shown in Figure 7a as a function of the two independent variables T and x_W, i.e., $v = f(T, x_W)$. The data points in this plot, $N_D = 345$, lie on a featureless near-to-flat surface.

The partial derivatives $(\partial v/\partial T)_{x_W}$ and $(\partial v/\partial x_W)_T$, treated as a function of T and x_W, obtained by Tikhonov regularization are shown in Figures 7b, c. As expected, $(\partial v/\partial T)_{x_W}$ is relatively small and the surface, apart from the trend of developing a small local maximum at low temperature, is quite featureless. $(\partial v/\partial x_W)_T$ is significantly larger and at low temperature shows a clear local maximum in the neighborhood of $x_W = 0.8$. Apart from the slight ripples at the boundaries of the measurement region, the surfaces of the partial derivatives appear to be well behaved.

$(\partial v/\partial T)_{x_W}$ and $(\partial v/\partial m_W)_T$ by themselves are not of particular physical interest but they are essential for the computation of the partial molar volumes $\overline{V}_W$ and $\overline{V}_{MIPA}$. At any temperature, these two thermodynamic variables are related to the partial derivative $(\partial v/\partial x_W)_T$ by[7]

$$\overline{V}_{MIPA}(T, x_W) = v - x_W\left(\frac{\partial v}{\partial x_W}\right)_T,\ \overline{V}_W(T, x_W) = v + (1 - x_W)\left(\frac{\partial v}{\partial x_W}\right)_T. \quad (10)$$

In these expressions, the specific volume $v(T, x_W)$, for any point in the measurement rectangle, is obtained by substituting the partial derivatives into Eq. 2 and performing line integral numerically. The resulting partial molar volume surfaces are shown in Figure 8a. They exhibit a local minimum or maximum in the neighborhood of $x_w = 0.8$ for some T. These are in agreement with the restricted partial molar volumes reported by Mokaroui et al.[6] and of Yeow et al.[8] In their computation, these authors treated the specific volume data at each measurement temperature as a function of single independent variable, i.e., $v = f(x_W)$ and obtained the ordinary derivative dv/dx_W from fitted expression[6] and from Tikhonov regularization computation,[8] respectively. They then used the ordinary derivative to compute the partial molar volumes at each of the measurement temperatures. A comparison of the partial volumes, as general functions of T and x_W, obtained in this investigation with those, as functions of x_w at the discrete measurement temperatures, obtained in the two earlier investigations is shown in Figure 8b. These plots show the partial molar volumes at $T = 353.15$, 283.15, 318.15K and, i.e., the highest, lowest measurement temperatures and their average. The continuous curves are the results from Eq. 7, the lighter broken curves are from Yeow et al.[8] and the discrete points are from Mokaroui et al.[6] The agreement among these results is indicative of the reliability of the partial derivatives in Figure 7b.

T-ρ-P *data of supercritical methane*

Trappeniers et al.[9] reported the pressure P of supercritical methane as a function of temperature T (between 273.16 and 423.16 K) and density ρ (between 13.23 and 410.91 kg

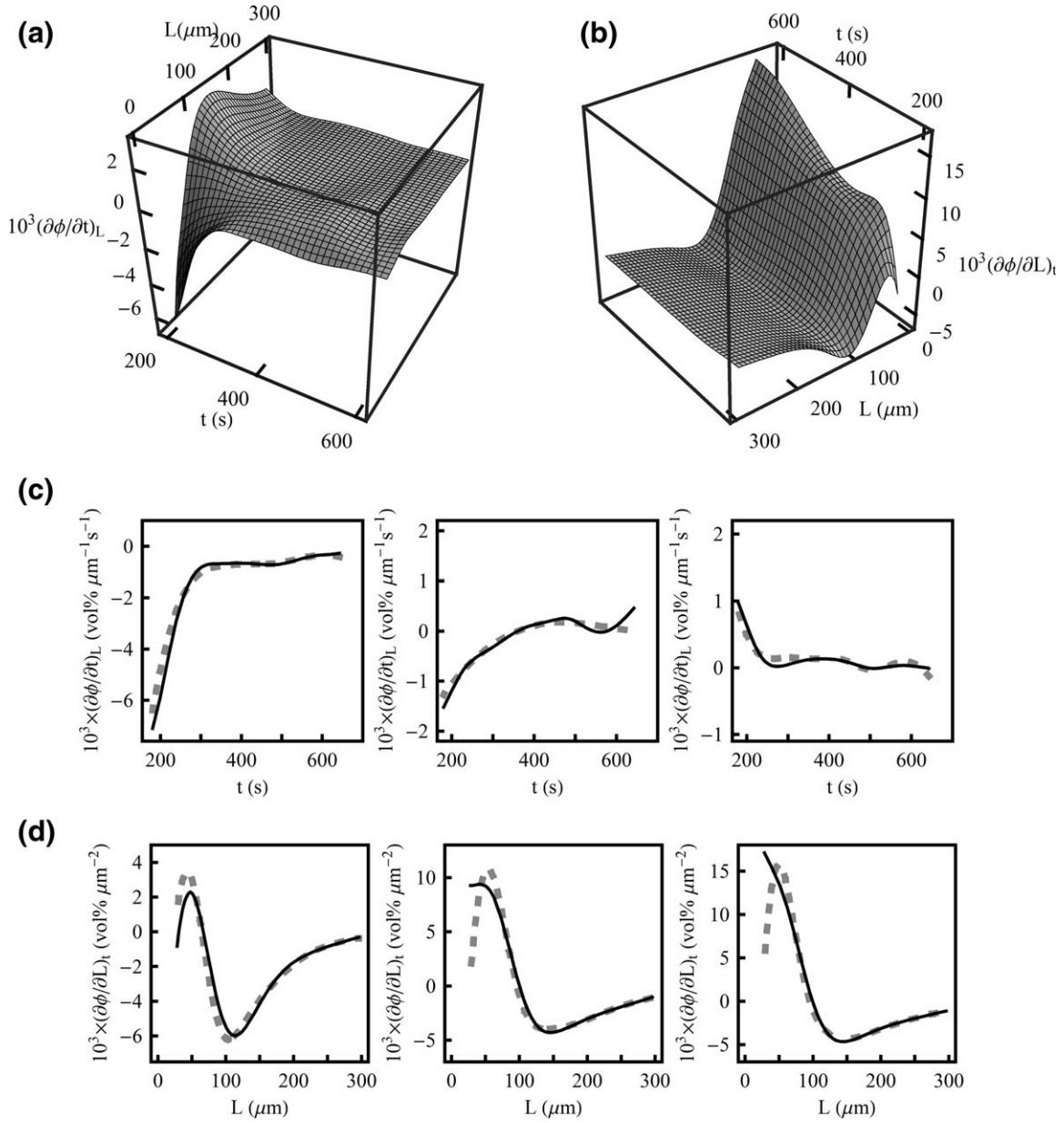

Figure 6. Computed derivatives of ϕ.

(a) Computed $(\partial\phi/\partial t)_L$ in vol % $(\mu m)^{-1}$ s^{-1}; (b) Computed $(\partial\phi/\partial L)_t$ in vol % $(\mu m)^{-2}$; (c) Comparison of $(\partial\phi/\partial t)_L$ (—) and $d\phi/dt$ (···), $L = 28.25$, 74.31, 295.83 (left to right) μm; (d) Comparison of $(\partial\phi/\partial L)_t$ (—) and $d\phi/dL$ (···), $t = 180$, 368, and 642 (left to right) s.

m^{-3}). Their data are shown as discrete points in Figure 9a and enlarged in Figure 9b for low ρ. In the present computation, those data points with $\rho > 269.14$ kg m^{-3} in the original data set of Trappeniers et al. have been left out and not shown in Figures 9a, b as these measurements do not cover the entire temperature range. $N_D = 408$ for this reduced T-ρ-P data set.

Adopting the same approach as in the previous examples, Eq. 7 was applied to compute the partial derivatives $(\partial P/\partial T)_\rho$ and $(\partial P/\partial\rho)_T$ for the measurement rectangle defined by $T_{min} = 273.16$ K $\leq T \leq T_{max} = 423.16$ K and $\rho_{min} = 13.23$ kg $m^{-3} \leq \rho \leq 269.14$ kg $m^{-3} = \rho_{max}$. Typical plots of these partial derivatives are shown as continuous curves in Figures 9c, d. The curves in Figure 9c are for T_{min}, $(T_{max} + T_{min})/2$, and T_{max}. Those in Figure 9d are for ρ_{min}, $(\rho_{max} + \rho_{min})/2$, and ρ_{max}. The computed partial derivatives over the region measurement rectangle have been substituted into Eq. 2 and integrated numerically to give the pressure P. This back-calculated P is shown in Figures 9a, b as continuous curves. The average difference between the back-calculated P and the experimental data is about 0.3%, which is the same order of magnitude as the error bars of the experimental data. However, it can be seen that at low ρ there is very perceptible deterioration in agreement.

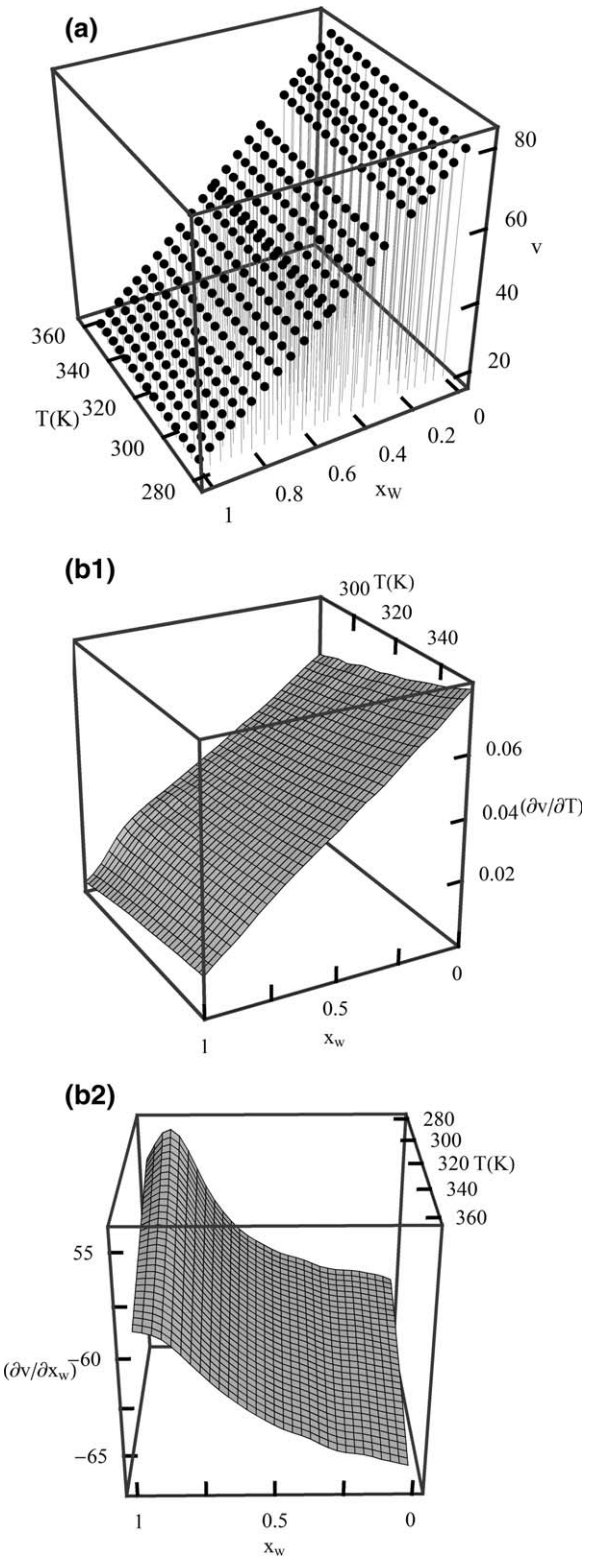

Figure 7. Properties of aqueous MIPA.

(a) Experimental v (cm^3 mol^{-1}) of Mokraoui et al.; (b) Computed surfaces of (b1) $(\partial v/\partial T)_{x_W}$ (cm^3 mol^{-1} K^{-1}) and (b2) $(\partial v/\partial x_W)_T$ (cm^3 mol^{-1}).

Setzmann and Wagner[10] have developed a single expression capable of representing a large number of the thermodynamic properties of methane. These properties include enthalpy, entropy, specific heat under different conditions, thermal expansion coefficient, compressibility, Joule-Thomson coefficient, isothermal expansion coefficient as well as pressure P over a very wide range of T and ρ. Their expression, adopted by IUPAC, consists of two series each with a large number of terms. The large number of parameters, well over 180, associated with these series were determined by least-squares fitting of the expression to a very large collection of thermodynamic properties taken from the literature. Their numerical values are tabulated in Setzmann and Wagner[10] and will not be repeated here. The resulting expression that gives P in terms of T and ρ has been differentiated with respect to the independent variables to yield $(\partial P/\partial T)_\rho$ and $(\partial P/\partial \rho)_T$. The partial derivatives generated this way are shown as light broken curves in Figures 9c, d. Apart from the boundary of the region analyzed, there is a very satisfactory agreement between the two sets of curves in each plot verifying the reliability of the results of Tikhonov regularization computation.

The isobaric partial derivative $(\partial \rho/\partial T)_P$ of fluids is of practical interest and appears explicitly in a number of thermodynamic identities. This partial derivative is related to the two partial derivatives of P, i.e., $(\partial P/\partial T)_\rho$ and $(\partial P/\partial \rho)_T$ by the standard mathematical relationship[3]

$$(\partial \rho/\partial T)_P = -(\partial P/\partial T)_\rho/(\partial P/\partial \rho)_T \tag{11}$$

The partial derivatives of methane generated by Eq. 7 are substituted into this equation and the resulting $(\partial \rho/\partial T)_P$ is plotted against ρ and shown as continuous curves in Figure 10a for $T = T_{max}$, T_{min}, and $(T_{max} + T_{min})/2$. The computed $(\partial \rho/\partial T)_P$ is also plotted against T for $\rho = \rho_{min}$ and ρ_{max} as well as a number of in between ρ. For comparison, the corresponding results obtained from the general expression of Setzmann and Wagner are again shown as broken curves on these plots. The agreement while satisfactory in general is showing signs of deterioration close to the boundaries of the measurement region. The deterioration is most significant for ρ close to ρ_{min} and ρ_{max} as can be observed from the curves for $\rho = \rho_{min}$ and ρ_{max} in Figure 10b. This is understandable as the error in the two partial derivatives $(\partial P/\partial T)_\rho$ and $(\partial P/\partial \rho)_T$ is amplified while applying Eq. 11.

Isothermal throttling coefficient $\psi \equiv (\partial h/\partial P)_T$ is a thermodynamic function of some practical importance. ψ which relates the change in specific enthalpy with pressure under isothermal condition can be measured directly in, for example, a flow calorimeter operating under isothermal mode. Through standard thermodynamic identities, it can be shown that ψ is given by

$$\psi \equiv (\partial h/\partial P)_T = [1 + (T/\rho)(\partial \rho/\partial T)_P]/\rho. \tag{12}$$

Thus, provided $(\partial \rho/\partial T)_P$ can be evaluated reliably, Eq. 12 provides a means of obtaining ψ from experimental T-ρ-P data. The $(\partial \rho/\partial T)_P$ from Eq. 11 and the back-calculated ρ shown in Figure 9 are now used in conjunction with this equation to obtain ψ. The outcome is plotted against T and shown as continuous curves in Figure 11a. On each of these curves, ρ is held fixed, between 50 and 250 kg m^{-3}. ψ can also be obtained from the general expression of Setzmann and Wagner. For comparison, this ψ is shown in Figure 11a

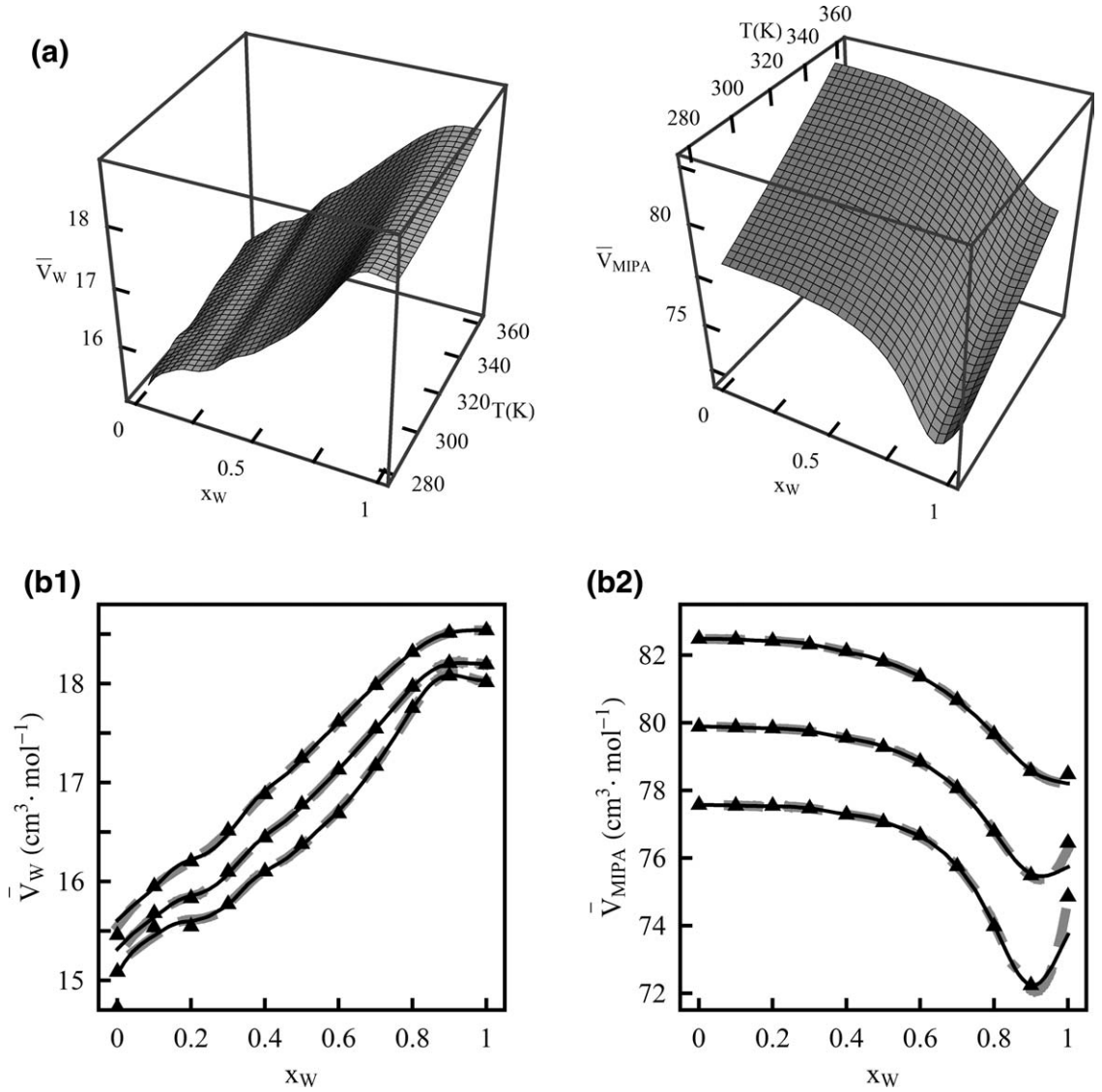

Figure 8. Partial molar volumes of aqueous MIPA.

(a) Surfaces of $\overline{V}_W$ and $\overline{V}_{MIPA}$ (cm^3 mol^{-1}); (b) Comparison of (b1) $\overline{V}_W$ and (b2) $\overline{V}_{MIPA}$ (cm^3 mol^{-1}) from Eq. 7 (——), Yeow et al. (—) and Mokraoui et al. (▲), $T = 283.15$ (lowest), 318.15, 353.15 (uppermost) K.

as light broken curves. There is a very satisfactory agreement between the two sets of ψ over the range of T and ρ shown in this plot. However, for $\rho_{min} < \rho < 50$ kg m^{-3} (not shown) there is very significant difference. The difference can be seen by plotting ψ as a function against ρ with T as an independent parameter. See Figure 11b. It is quite clear that, for $\rho_{min} < \rho < 50$ kg m^{-3}, the results based on the results of Tikhonov regularization are erroneous. This failure can be traced to the poor performance of the back-calculated ρ close to ρ_{min}, see Figure 9b, and also to the accumulated error in $(\partial\rho/\partial T)_P$, which is further amplified by the small numerical value of ρ in this region.

Discussion

The derivation of Eq. 7 involves a sequence of steps that may appear complicated. But all of the steps involved are relatively direct and intuitively obvious. For example, the grouping of the unknowns into **P** and the combining of the matrices of coefficients to form composite matrices **C** and **E** may appear convoluted but the resulting simplification in the formulation and in the solution processes leading to Eq. 7 is self evident. Furthermore, all the matrix manipulation steps leading to and in Eq. 7 can be handled automatically by scientific computing software with symbolic manipulation capability requiring little or no physical intervention.

Experience shows that the setting up of the matrices **A** and **B** in Eq. 4, **D** in Eq. 6, and **β** in Eq. 7 require some planning. All these are sparse or very sparse matrices. As already mentioned, the locations of the non-zero elements in them depend on the way the discretization points in the two-dimensional grid are numbered. Computer-assisted book keeping of the immediate neighbors of a general grid point

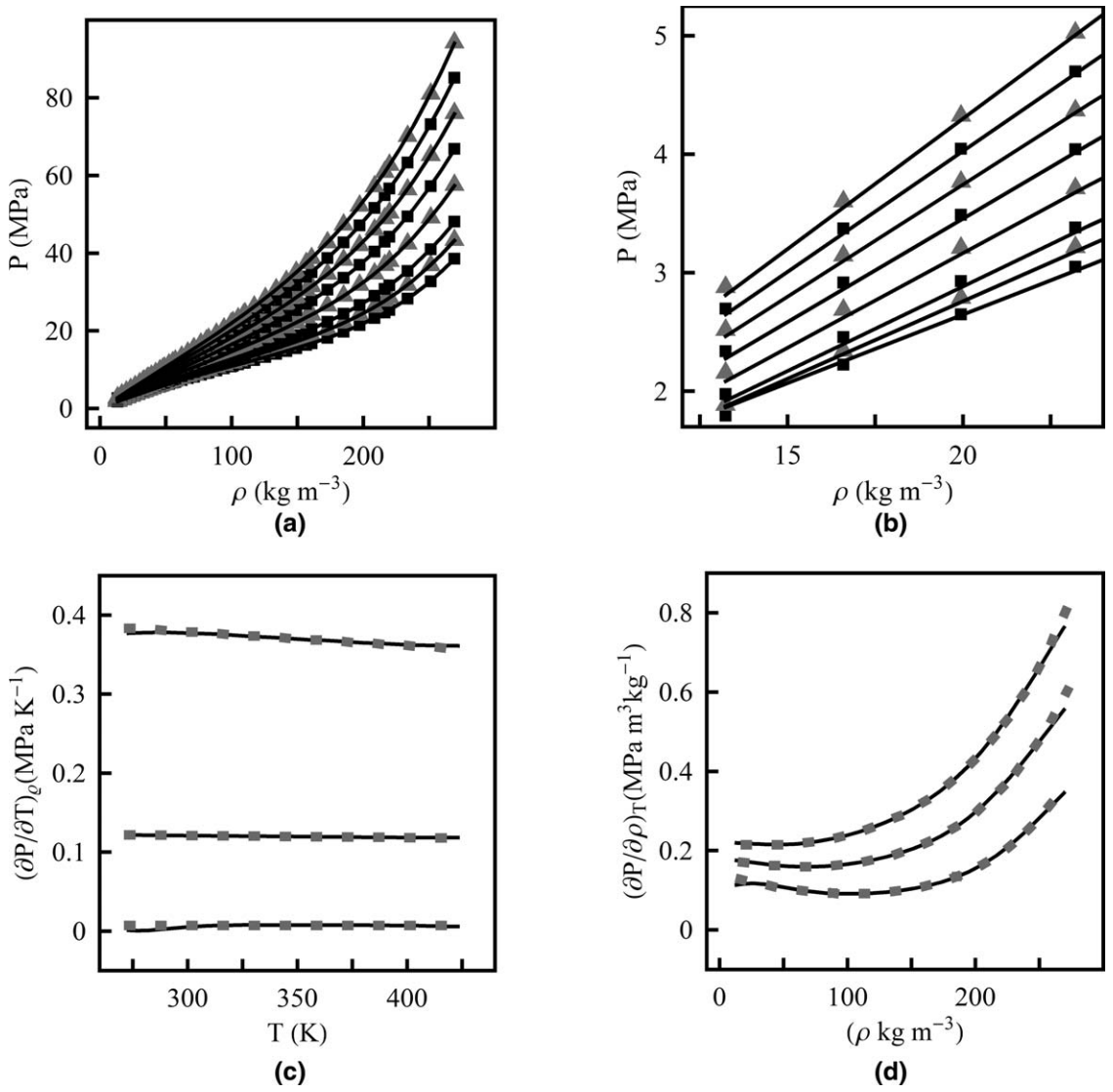

Figure 9. *T*-ρ-*P* data and partial derivatives of methane.

(a) P from Trappeniers et al. (■ and ▲) and that back calculated from Eqs. 7 and 2 (——) plotted against ρ for $T = 273.16$ (lowest), 285.66, 298.16, 323.16, 348.16, 373.16, 398.16, 423.16 (uppermost) K; (b) Enlargement of (a) for low ρ; (c) $(\partial P/\partial T)_\rho$ from Eq. 7 (——) and from Setzmann and Wagner (▪▪▪) plotted against T with $\rho = 13.23$ (lowest), 141.18, 269.14 (uppermost) kg m^{-3}; (d) $(\partial P/\partial \rho)_T$, legend as in (c), plotted against ρ with $T = 273.16$ (lowest), 348.16, 423.16 (uppermost) K.

and the identification of the grid points on the four boundaries are clearly critical to this step. Another critical step is the identification of the intersection points of the integration path in Eq. 2 with the gridlines and the evaluation of the weighting factors in the linear interpolation processes shown in Figure 1. Experience again shows that scientific computing software with symbolic manipulation capability is ideal for this task.

Equation 7 that converts general experimental data of two independent variables into partial derivatives is of the same form as the equation of Lubansky et al. that converts experimental data of one dependent variable into ordinary derivatives. In both cases, the key computation operations are matrix transposing, matrix multiplication, and matrix inversion all of which can be performed using commercial scientific computing software. In the case of ordinary derivative, typically the number of data points N_D is of the order of 50 and the total number of discretization points N_T ($= N_K$) and hence the number of unknowns involved is around 200. The resulting matrix operations can be handled with ease by a 2 GHz computer and the time required is no more than a few minutes inclusive of post processing and result presentation. For the partial derivative problem, the magnitude of the computation operations is much larger. For example, to achieve reliable outcome, the number of data point has to be much larger compared to those in ordinary derivative problems, typically $N_D = 250$. With a modest $N_K = 41$, the number of discretization points $N_T = 1681$ and the corresponding number of unknowns (i.e., size of $\mathbf{P}$) $= 3363$. These are an order larger than that encounter in ordinary derivative problems. The size of matrix $\mathbf{E}$ and that of $\boldsymbol{\beta}$ in Eq. 7 are 1722 $\times$ 3363 and 6396 $\times$ 3363, respectively. It was found that,

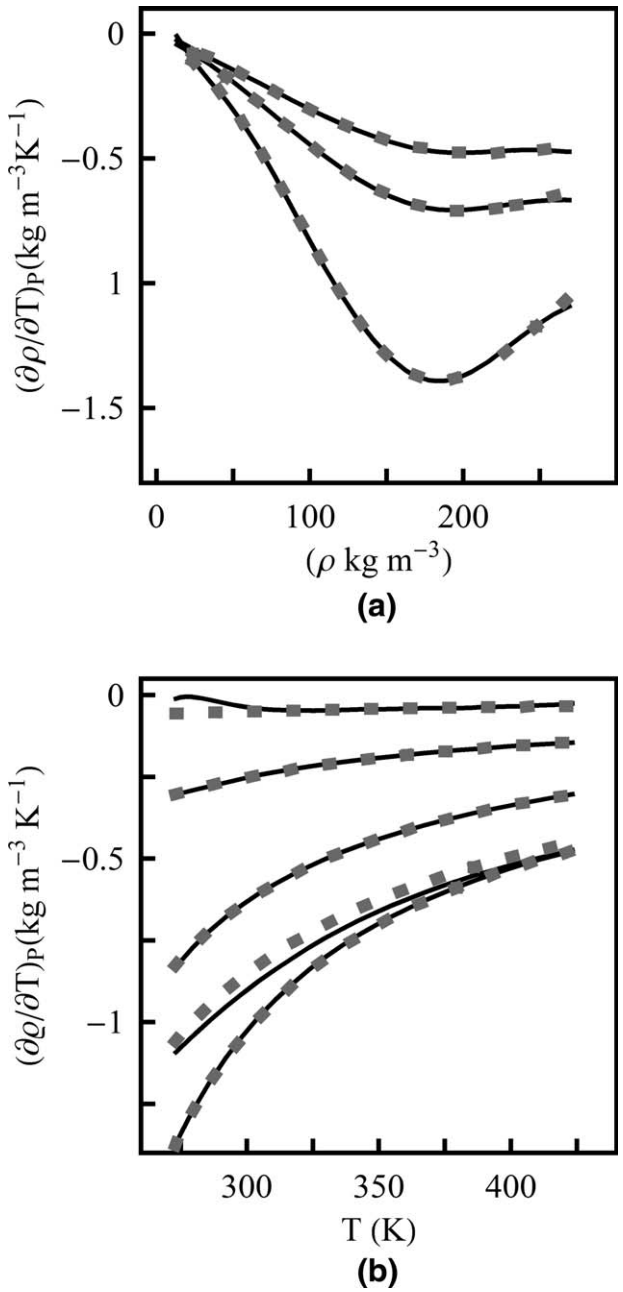

Figure 10. Isobaric derivative of ρ.

(a) $(\partial\rho/\partial T)_P$ from Eq. 7 (——) and from Setzmann and Wagner (···) plotted against ρ for T = 273.16 (lowest), 348.16, 423.16 (uppermost) K; (b) As in (a) but plotted against T for ρ = 13.23 (uppermost), 50, 100, 269.14, 200 (lowest kg m^{-3}).

using the general routines provided by commercial scientific computing software, the matrix operations in Eq. 7 can take as long as 30 min on a 2 GHz computer. In execution of the examples shown above with a 2 GB RAM computer, depending on the background tasks, it was observed that the computer can occasionally run out of memory. As 4 GB RAM computers and the associated operating system now becoming more common computing time and memory requirements are unlikely to be a continued issue. If Eq. 7 is to be routinely applied or applied to even larger data sets then exploiting the sparse nature of most of the matrices would be the most effective way of reducing the storage requirements and the speeding up of the computation of the partial derivatives. This has not been attempted in the current investigation.

In all the examples considered, the choice of the regularization parameter λ was guided by the Morozov Principle. As in the case of ordinary derivative, it was found that guided by physical knowledge of the problem, this simple and intuitively obvious approach appears to perform satisfactorily. Other techniques commonly used to guide the choice of λ

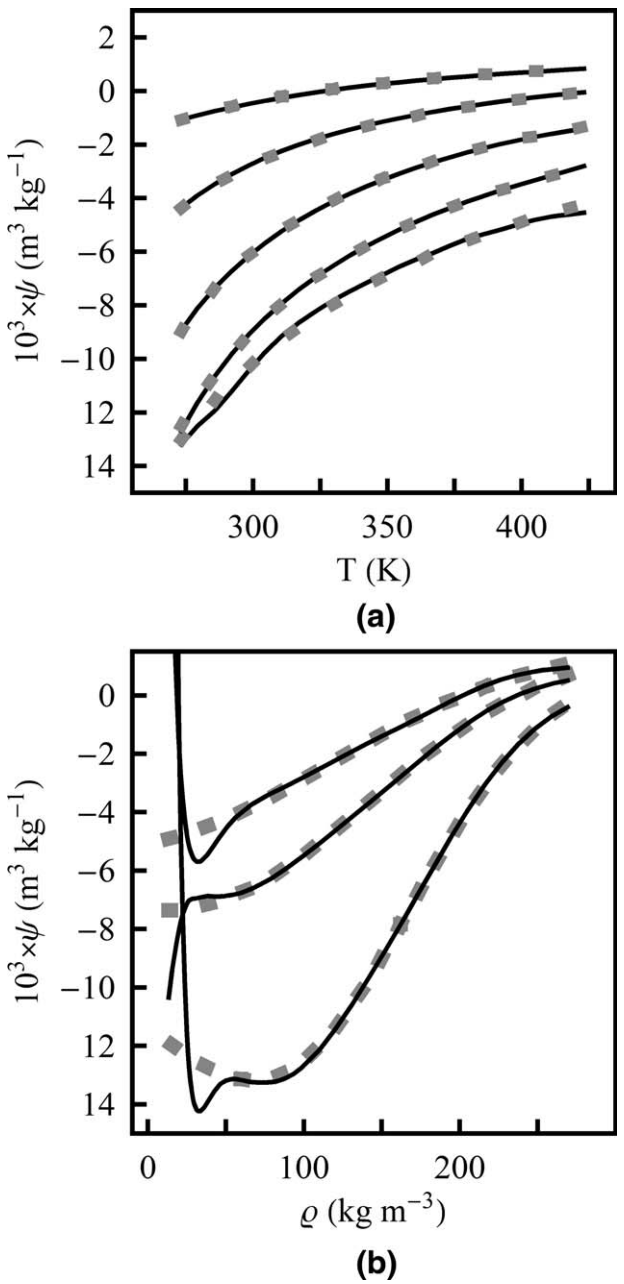

Figure 11. Isothermal throttling coefficient.

(a) From Eq. 7 (——) and from Setzmann and Wagner (- - -) plotted against T for ρ = 50 (lowest), 100, 150, 200, 250 (uppermost) kg m^{-3}; (b) As in (a) but plotted against ρ for T = 273.16 (lowest), 348.16, 423.16 (uppermost) K.

include the L-curve Method[11] and the method of Generalized Cross Validation (GCV)[12]. Extending these methods to the partial derivative problem will require investigation and will increase further the computing resources required. This too has not been attempted.

Limited numerical experimentation has been carried out on the possible ways of improving the reliability of the derivatives towards the boundary of the measurement region. It was found that by reducing λ it is possible to reduce the differences between the computed partial derivatives close to the boundaries and their expected values. However, this is generally accompanied by the appearance of spurious fluctuations spreading from the boundary region towards the interior. Clearly, the choice of λ becomes a question of balancing these two trends and the results shown above represent as what is considered to be an appropriate but subjective choice. The deterioration near the boundaries may be linked to the fact that the mixed second derivative requirement of Eq. 1 has not been applied at the grid points on the boundaries. Nor has the minimization of the second derivatives been applied in full at these boundary gird points. It is possible to impose these conditions at additional points not on the regular gridlines but at $\Delta/2$ distance, on the interior side, from the boundaries without bringing in unknowns exterior to the measurement region. The efficacy of such an extension has not been investigated as this is not in tune with the adopted practice of using the simplest and consistent finite approximation scheme when applying Tikhonov regularization to deal with ill-posed inverse problems.[1]

Given a discrete set of experimental measurements one often requires the value of the dependent variable at locations which do not coincide with the measurement points. In the case of experimental data with a single independent variable, the commonly adopted practice is to interpolate the required value using a least-squares fitted curve of some form. The issues one is then immediately confronted with are the selection, from a large number of possible candidates, of the form of function to be use and how the least-squares fitting is to be carried out, whether globally or the number of points per fitting if performed locally. These are issues that do not have simple and general answers.[13] When extended to data with two independent variables, the same issues remain and they are now associated with surfaces instead curves. Their solution becomes even more troublesome and less well defined. As have been demonstrated above, substituting the partial derivatives from Eq. 7 back into Eq. 2 and performing the line integration numerically allows one to obtain the dependent variable with, in most cases, a high degree of accuracy. This procedure has the very significant advantage that it is independent of any assumed functional relationship between the dependent variable and the two independent ones. This result is also global since the Eq. 2 is valid for any point within the measurement region. This is a spinoff from the present investigation that will find immediate and widespread practical applications.

Conclusion

Apart from the deterioration in performance close to the boundary region of the measurement rectangle, the method based on Tikhonov regularization is a reliable way of obtaining the first partial derivatives of experimental data of two independent variables. The method is general in that it does not require the functional relationship between the variables to be known or assumed. The procedure can also be used as a general purpose interpolation tool of two-dimensional data.

Acknowledgments

The authors are grateful to Binbing Han, Ranil Wickramasinghe, and Jong-Leng Liow for the experimental data used in the yeast flocculation example.

Literature Cited

1. Engl HW, Hanke M, Neubauer A. *Regularization of Inverse Problems*. Dordrecht, The Netherlands: Kluwer, 2000.
2. Lubansky AS, Yeow YL, Leong Y-K, Wickramasinghe SR, Han B. A general method of computing the derivative of experimental data. *AIChE J*. 2006;52:323–332.
3. Riley KF, Hobson MP, Bence SJ. *Mathematical Methods for Physics and Engineering*, 2nd ed. Cambridge, UK: Cambridge University Press, 2002.
4. Randolph AD, Larson MA. *Theory of Particulate Processes: Analysis and Techniques of Continuous Crystallization*, 2nd ed. San Diego: Academic Press, 1988.
5. Han B, Wickramasinghe SR, Liow JL. Unpublished data. 2006.
6. Mokraoui S, Valtz A, Coquelet C, Richon D. Volumetric properties of the isopropanolamine: water mixture at atmospheric pressure from 283.15 to 353.15K. *Thermochim Acta*. 2006;440:122–128.
7. Sandler SI. *Chemical Biochemical and Engineering Thermodynamics*, 4th ed. New York, NY: Wiley, 2006.
8. Yeow YL, Ge J, Leong Y-K, Khan A. Investigating the properties of aqueous monoisopropanolamine using density data from 283.15K to 353.15K. *Int J Thermophys*. 2009;30:448–463.
9. Trappeniers NJ, Wassenaar T, Abels JC. Isotherms and thermodynamic properties of methane at temperatures between 0°C and 150°C and at densities up to 570 Amagat. *Physica*. 1979;98A:289–297.
10. Setzmann U, Wagner W. A new equation of state and tables of thermodynamic properties for methane covering the range from the melting line to 625 K at pressures up to 1000 MPa. *J Phys Chem Ref Data*. 1991;20:1061–1155.
11. Hansen PC. Analysis of discrete ill-posed problems by means of the L-curve. *SIAM Rev*. 1992;34:561–580.
12. Wahba G. *Spline Models for Observational Data*. Philadelphia, PA: SIAM, 1990.
13. Dierckx P. *Curve and Surface Fitting with Splines*. Oxford, UK: Oxford University Press, 1993.

Manuscript received Nov. 17, 2009, and revision received Feb. 11, 2010.